PAN

Opto-Electronics Review

journal homepage: https://journals.pan.pl/opelre

Compact terahertz devices based on silicon in CMOS and BiCMOS technologies

Dmytro B. But[1,2*], Alexander V. Chernyadiev[1], Kęstutis Ikamas[3,4], Cezary Kołaciński[1,5], Anastasiya Krysl[6], Hartmut G. Roskos[6], Wojciech Knap[1], Alvydas Lisauskas[1,3]

[1]CENTERA, Institute of High Pressure Physics of the Polish Academy of Sciences, Sokolowska 29/37, 01-142 Warsaw, Poland
[2]NOMATEN Centre of Excellence, National Centre of Nuclear Research, A. Soltana 7, 05-400 Otwock-Świerk, Poland
[3]Institute of Applied Electrodynamics and Telecommunications, Vilnius University, Saulėtekio Av. 9, LT-10222 Vilnius, Lithuania
[4]General Jonas Žemaitis Military Academy of Lithuania, Šilo Av. 5A, LT-10322 Vilnius, Lithuania
[5]Łukasiewicz Research Network Institute of Microelectronics and Photonics, Al. Lotników 32/46, 02-668 Warsaw, Poland
[6]Institute of Physics, Goethe University Frankfurt, Max-von-Laue-Str. 1, D60435 Frankfurt, Germany

Article info

Article history:
Received 21 Jan. 2023
Received in revised form 21 Feb. 2023
Accepted 22 Feb. 2023
Available on-line 18 Apr. 2023

Keywords:
Terahertz; teraFET; CMOS; THz emitter; THz detectors.

Abstract

This paper reports on compact CMOS-based electronic sources and detectors developed for the terahertz frequency range. It was demonstrated that with the achievable noise-equivalent power levels in a few tens of pW/√Hz and the emitted power in the range of 100 µW, one can build effective quasi-optical emitter-detector pairs operating in the 200–266 GHz range with the input power-related signal-to-noise ratio reaching 70 dB for 1 Hz-equivalent noise bandwidth. The applicability of these compact devices for a variety of applications including imaging, spectroscopy or wireless communication links was also demonstrated.

1. Introduction

There is a continuous growth of interest in signal generation and detection at the millimetre-wave and terahertz (THz) frequency ranges. The electromagnetic radiation at these frequencies can penetrate through many materials while having non-ionizing photon energies; furthermore, many compounds and materials possess characteristic spectral absorption lines, which allow for their unique identification [1]. Strong motivation for new technological developments also comes from the demand to increase data transfer speed in wireless communications [2]. However, for THz technologies to become applicable in large-scale consumer-oriented applications, there is a strong demand for compact, cost-effective, high-performing technology solutions operating at room-temperature conditions. Most existing THz systems which are used to provide proof-of-principle for the uniqueness of this frequency range are based on large and not scalable discrete elements: electronic multipliers which involve high technological effort demanding waveguides [3, 4], bulky solid-state pulse laser-driven time-domain spectroscopy (TDS) systems [5], laser-driven photomixers [6], slow Golay cell [7], optoacoustic [8] or pyroelectric device [9], or even cryogenically-cooled bolometers [10].

The status quo with THz technologies being limited mainly to laboratory applications might change rather soon [11]. It is driven by the development of new component concepts which enable the operation in the THz frequency range for devices fabricated using mainstream semiconductor device fabrication technologies such as the complementary metal-oxide-semiconductor (CMOS) technology. This technology high yield and repeatability allow the implementation of power-combining techniques using integrated array antennas for increasing output power [12]. It has already been demonstrated that THz detectors implemented in CMOS technologies are already competitive with the established state-of-the-art detection approaches [13]. In contrast, the performance of devices for generation is steadily improving and approaching the power levels which become competitive to those achievable with III/V-material system-based devices [14, 15].

In this manuscript, one of the leading concepts recently employed for detecting (section 2) and generation (section 3)

*Corresponding author at: dbut@unipress.waw.pl

https://doi.org/10.24425/opelre.2023.144599
1896-3757/ Association of Polish Electrical Engineers (SEP) and Polish Academic of Sciences (PAS). Published by PAS

of THz radiation in CMOS-based technologies will be addressed. Different CMOS-based emitter–detector pair operation modalities (section 4) will be discussed including data transmission, spectroscopy, and imaging applications.

2. Detectors

The functional performance of a detector can be described in many different ways. The ratio between the internal noise amplitude and the detector responsivity defines one. This metric is called noise-equivalent power (NEP) [16] and could be used as the figure of merit for the comparison of different detectors in the same frequency range. The efficiency of Schottky diodes [17], RTD [18], or field-effect transistors (FET)-based THz detectors (TeraFET) [19] depend on their nonlinear electric conduction properties, which enable them to rectify an AC-current that is induced by the incoming high frequency radiation.

High scientific interest in the THz frequency range resulted into invention and demonstration of a plethora of new materials and methods. For example, efficient detection has been proven due to thermoelectric effect in graphene [20, 21], ballistic rectification [22], self-switching diode rectification [23], photoelectric effect in Si [24], rectification in tunnel field effect transistors using bi-layer graphene [25], and many others.

Here, the focus was put on the case of TeraFET devices for which the asymmetric coupling of radiation between the drain and source terminals of the transistor channel leads to the formation of induced voltage proportional to the radiation power, i.e., the photovoltaic effect [26]. There are multiple ways to induce the asymmetry between the drain and source terminals [27], but the architectures of transistors directly connected to on-chip integrated antennas are the most effective.

The first findings relevant to the successful application of CMOS-fabricated FET-based devices for efficient detection of THz radiation were reported in 2009 [28]. This work demonstrated the implementation of the plasmonic mixing concept earlier proposed by Dyakonov and Shur [26, 29] in a standard CMOS foundry technology [28]. Since then, the understanding of device properties and concomitant performance of CMOS-based detectors were constantly improved. By now, it is in direct competition with the performance values previously accessible only for mature Schottky diode technology [30–32].

Since the first demonstration of FETs in THz imaging [27, 33], utilizing FET-based detectors for the THz frequency range is still evolving. The current success, as well as further performance improvements, are strongly related to the general development in the field of high-frequency integrated circuits and correlate with the maturity of the technology allowing for optimization of THz radiation coupling by the monolithic implementation of antennas, as well as reduction of parasitic capacitances or serial resistances. The exceptional maturity of silicon technologies allows the integration of antennas with resonances going deep into the THz frequency range [19, 32].

The two most common schemes of radiation coupling schemes forming a number that is already presented in the literature are shown in Fig. 1(a) and 1(b): (a) gate-driven [19] and (b) differentially source-driven [34], where V_{THz} is the voltage induced by THz radiation, Z_{ant} is the antenna impedance, V_g is the gate bias, V_{det} is the rectified signal, L_g and L_{tl} are the parasitic inductance of the gate and drain, respectively. For both of them, ensure that the induced oscillations are launched from only one side of the gated transistor channel, where induced high-frequency waves die out at the channel beginning regardless of the load at the other end and present equivalent intrinsic rectification efficiency. The gate-driven configuration is a typical choice in detectors connected to bowtie or patch antennas. The differential source-driven scheme consists of two transistors with their drains and gates connected, respectively. The out-of-phase THz signal is coupled to each of the two sources of the differential pair. Drains are also coupled, and this port is output for rectified signal. The schematic better matches impedances between the antenna and detectors and could be used for a wide-band detector operation.

Implementing an efficient antenna in the THz integrated detector is one of the main challenges in the device development process. CMOS Si TeraFET detectors commonly use planar antennas as bowtie antennas, slot-dipole antennas, and spiral antennas. These antennas require a substrate lens [see Fig. 1(d)] since most of the power of an on-chip planar antenna is directed into the silicon substrate because of its lower intrinsic impedance compared to air. An example of broadband planar antenna response is shown in Fig. 2(a) by the green curve compared to the radiation from the cw-photomixer THz source, the red curve. Such devices are reported to demonstrate a broadband operation with nearly flat frequency response from 400 GHz up to 1.5 THz [30] (now, this range is extended up to 2.7 THz). They can be utilized with low-average-power sources for THz radiation, like photomixers [35] or photoswitches [36], as well as with high-power molecular optically pumped THz lasers [37]. A recent study [13] dedicated to the sensitivity issues of nanometric field effect transistors as THz sensors is worth mentioning.

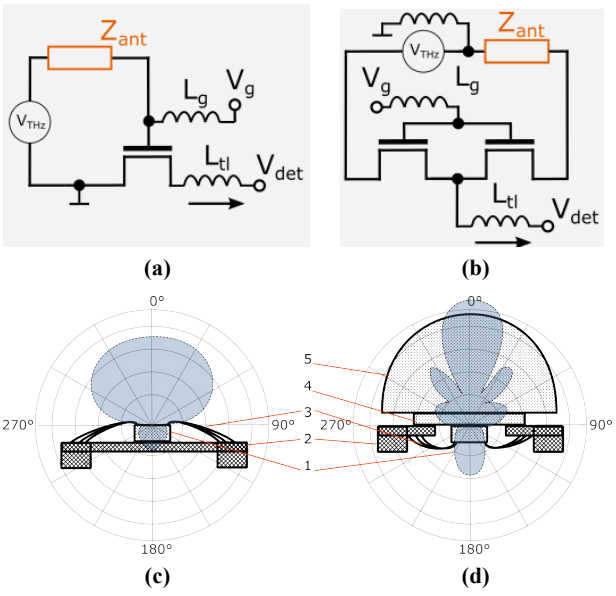

Fig. 1. Common architectures to couple THz radiation into the transistor channel: (a) gate-driven, (b) differentially source-driven. Examples of radiation patterns (φ = 0°) of (c) patch antenna and (d) planar substrate-based antenna, where 1 is the die with integrated structure, 2 is the sample holder-based with contact pads, 3 is the wire bonding, 4 is the transparent substrate, 5 is the substrate lens.

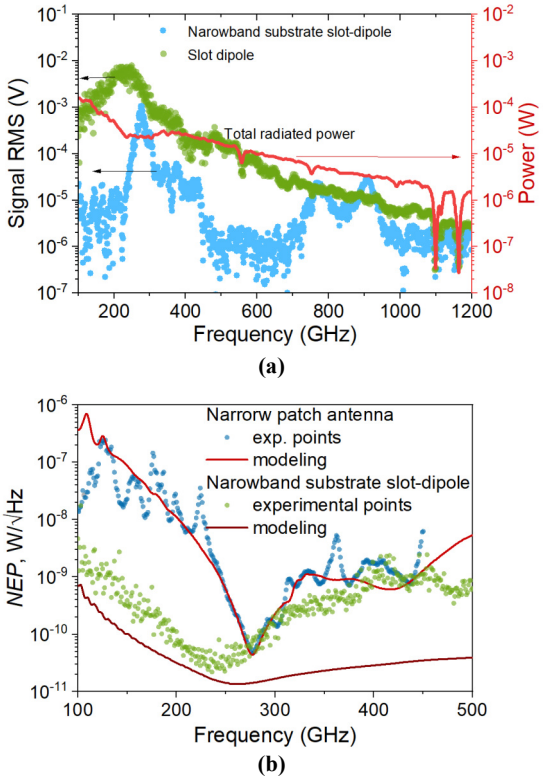

Fig. 2. (a) Comparison of voltage response as a function of the frequency for CMOS-based TeraFET with a narrowband patch antenna (blue dots) and the substrate-lens coupled (green dots) slot dipole antenna. The red curve is the power of cw-photomixer THz radiation source. (b) Comparison of NEP for narrowband patch (blue dots) and slot dipole (green dots) antennas as a function of frequency. The red curves correspond to the calculated value of NEP for respective devices.

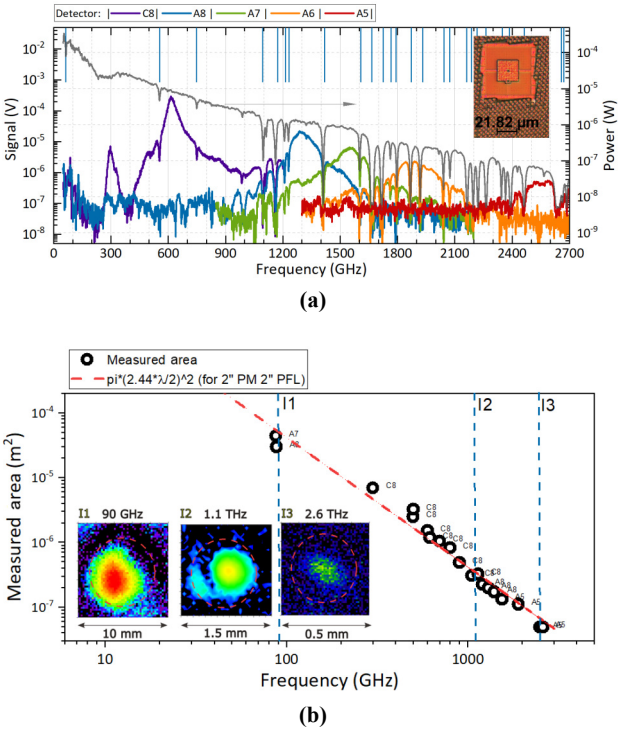

Fig. 3. (a) The power spectrum of the cw-photomixer THz radiation source is denoted by the grey curve, with the blue vertical lines indicating the water absorption lines. The colour curves correspond to signals that have been measured utilizing a TeraFET detector with patch antennas. (b) Beam areas as a function of the frequency that was determined during experiment [see panel (a)]. The insert displays examples of raster scans conducted using TeraFET with a patch antenna at different frequencies (blue dashed lines), with the scale of the scan area provided.

The second common solution are patch antennas with on-chip ground planes that radiate towards the top chip-to-air interface [see Fig. 1(c)]. The response of this antenna type is presented in Fig. 2(a) by the blue curve. The key features of the patch antenna are a narrowband bandwidth and a relatively low directivity compared to a planar antenna with a substrate lens (see the schematic view in Fig. 1(c) and 1(d). The patch antennas vertical and horizontal beamwidth (−3 dB level) could achieve 60° [38]. Devices based on patch antennas could be used as point detectors since the lowest-order resonance mode, TM_{10}, occurs when the effective length of antenna is equal to half the wavelength. This property of the antenna is beneficial, as it allows operation below the diffraction limit of quasi-optical components in a measurement system. Figure 3(a) presents signals of TeraFET patch detectors for different resonant frequencies. The spectra lines of patch antenna devices in Fig. 3(a) are colour-coded based on their central resonance frequencies, which are as follows: C8: 620 GHz – violet, A8: 1300 GHz – blue, A7: 1550 GHz – green, A6: 1880 GHz – orange, and A5 – 2600 GHz – red. The blue vertical lines correspond to water absorption lines in the atmosphere. The inset of Fig. 3(a) shows one of the structures with a scale marker. Figure 3(b) demonstrates the dependence of the Gaussian beam profile area on the frequency. The profiles were recorded using detectors with patch antennas, which have the resonances at the appropriate frequencies (compare with data in Fig. 3). Detectors were placed at the focal point of a 2″ diameter parabolic mirror (PM) with a 2″ parent focal length (PFL). The inset of Fig. 3(b) gives an idea about the profile view at different frequencies with scales of raster scans for each frequency. The red dotted line represents the analytical dependence of the beam diameter in the quasi-optic system that was used.

The efficiency of radiation coupling by integrated patch antennas can be boosted by a dielectric lens [39]. This lens is placed on top of a plane antenna. It raises the detector performance by increasing the effective area but could simultaneously shift resonance frequency depending on the lens material dielectric properties [40].

Figure 2(a) compares voltage responses of CMOS-based TeraFET detectors with different antennas. The noise voltage for both detectors is about 8 nV/√Hz, and the dynamical range at the peak of responsivity is 60 dB for the equivalent noise bandwidth of 1 Hz, referring to the power of the THz radiation (120 dB referring to the voltage signal at the output). Figure 2(b) compares the measured NEP for both detectors with the calculated one. Methods of NEP calculation for TeraFETs with different types of antennas were described in Ref. 13. Both detectors, broadband and narrowband one, have similar values of NEP at the same frequency, 280 GHz, which means that both approaches are compatible and could be effectively used, corresponding to application requirements.

3. Sources

Traditionally, silicon CMOS technologies are optimized for digital applications and, therefore, are not seriously considered for THz frequency applications due to their limited maximum frequency of oscillation f_{max}. However, the continuous device scaling and the development of bipolar CMOS (BiCMOS) devices have already contributed to the paradigm shift and enabled CMOS technologies to enter the THz range.

3.1. Colpitts oscillator basics

The first reported CMOS-based sources emitting in the THz frequency range employed the cross-coupled transistor pairs [41–43]. In order to optimize the performance of circuits at high frequencies, there were several routes of improvements: by including buffer amplifying elements [44], by extending to multiple-push configurations [45], or by employing a differential Colpitts oscillator configuration, which gained popularity over time. A typical schematic of the Colpitts oscillator in a common-source configuration is presented in Fig. 4(a) [46]. The general functionality requires only a single amplifying element (it can be either a FET as in the example, a bipolar transistor in an amplifier stage), one inductor L and two capacitances C_1 and C_2. The oscillation frequency is defined by the resonant circuit formed by the inductor and the capacitance value resulting from the in-series connection of capacitances C_1 and C_2:

$$f_{res} = \left(2\pi\sqrt{LC_1C_2/(C_1+C_2)}\right)^{-1}. \quad (1)$$

This topology allows including a comparatively large load into the drain sub-circuit, which, on the other hand, reduces the requirement to maintain the high-quality factor of the resonant circuit. The main disadvantage of the simple circuit described in Fig. 4(a) is a requirement for a voltage gain to exceed 4 to sustain stable oscillations. However, the latter condition can be eased by at least two measures, one of which is separating the gate terminal from the ground by introducing an additional inductance L_g as presented in Fig. 4(b), and the second – by implementing a differential topology with two transistors M_1 and M_2 as presented in Fig. 4(c).

Figure 4(b) presents the modified high-frequency equivalent circuit of the Colpitts oscillator. Furthermore, since the highest resonant frequency can be achieved by implementing the lowest possible LC product, an external capacitor C_1 can be fully omitted. Its role is taken by the intrinsic capacitance formed between the drain and source terminals C_{DS}. At the usual biasing conditions, which can be assumed as $C_{GS} \gg C_{GD}$ to be valid, a simple analysis predicts the resonant frequency

$$f_{res} = \frac{1}{2\pi\sqrt{C_{DS}\dfrac{L_dC_2 + C_{GS}(L_d+L_g)}{C_{DS}+C_2+C_{GS}}}}. \quad (2)$$

It is worth noting that the additional inductor L_g connected to the gate terminal reduces the requirement for the gain, however, it also enables oscillations to take a different current path [47] and, therefore, requires thorough consideration. The analysis of the oscillator circuit can be

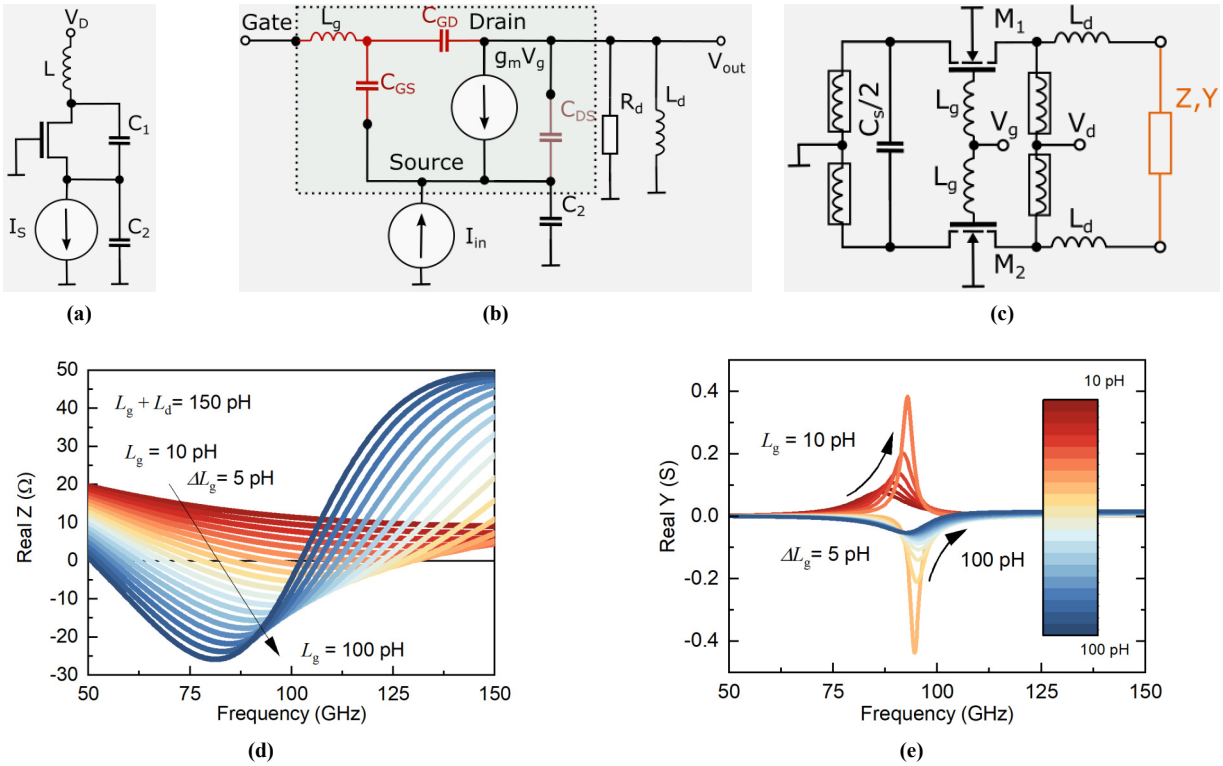

Fig. 4. (a) Schematics of a Colpitts oscillator in common-base configuration. (b) The equivalent small-signal schematics of Colpitts oscillator. (c) A circuit with two symmetrically combined Colpitts oscillators based on identical transistors $M1$ and $M2$ can be analysed as a two-terminal device with negative impedance Z. Finally, (d) the simulated impedance for a MOSFET with 60 nm gate length and 28 µm width (14 fingers with 2 µm each), and (e) the spectrum of the real part of conductance for different values of L_g.

greatly simplified using a push-push configuration which involves two symmetrically combined modified Colpitts oscillators based on similar transistors M_1 and M_2 [see Fig. 4(c)]. From the load perspective, this circuit can also be considered as a two-terminal device with the negative impedance Z or conductance Y. For the illustration, in Fig. 4(d) and 4(e), we present the results of simulations when the transistors M_1 and M_2 are MOSFETs with a 60 nm gate length and a 28 µm width (14 fingers with 2 µm each, with $f_{max} = 162$ GHz) with a fixed valued $L_g + L_d$ equal to 150 pH and L_g varied from 10 pH to 100 pH by a step of 5 pH. The simulations demonstrate that when the gate inductance L_g becomes large, the real part of impedance starts to be negative and its minimal value shifts to lower frequencies. However, the minimal value of the real part of conductance remains nearly independent of frequency which also corresponds to a resulting oscillation frequency of 94 GHz. Furthermore, the modelling indicates that by careful selection of inductance and source capacitance values, the schematic enables achieving stable fundamental oscillations up to 140 GHz, i.e., close to 0.8 f_{max} .

3.2. *Performance of implemented devices*

Simplified schematics for a harmonic push-push oscillator implemented in a 65 nm CMOS technology are presented in Fig. 5(a). It uses two 28 µm wide transistors (14 fingers, each 2 µm wide) with 60 nm long channels. The drain inductor at 84 GHz fundamental frequency has about 140 nH inductance, whereas, at the third harmonic, its complex impedance approaches $69+21i$. In order to enhance the radiative properties, the inductor has a bowtie shape, as presented in the inset of Fig. 5(c). The spectrum of radiated power at three different drain-to-source bias voltages is presented in the main panel of Fig. 5(c). The oscillator demonstrates a 3 dB tuning range from about 252 GHz to 259 GHz. More details about this design and device characteristics can be found elsewhere [48].

The same concept of the push-push type of oscillator can also be optimized for the emission of fundamental harmonics. An oscillator for a 130 nm BiCMOS process for this task was designed. A similar schematic, but now involving a pair of bipolar transistors, is presented in Fig. 5(b). The shape of the drain inductor has been derived from a bowtie antenna with a shorting element near the neck of the antenna to provide an inductive character of impedance near the target frequency of 250 GHz. The micrograph of the implemented circuit is shown in the inset of Fig. 5(d). Similarly, as for the previous example, the dependence of the radiated power into the free space at different bias conditions measured with a calibrated detector is presented in Fig. 5(d). When biased with 1.4 V to the collector terminal and 1 V to the gate terminal, the circuit delivers up to 325 µW of propagating power and the 3 dB tuning range from 258.5 GHz to 263 GHz. Although the achieved tuning range is narrower than for CMOS devices, the advantage of operating at fundamental frequency allows achieving about 3 times larger emitted power with the additional improvement by about the factor of two if the absorption in a doped substrate and Fresnel reflection loss would be minimized.

3.3. *State-of-the-art for CMOS-based THz oscillators*

Based on the state-of-the-art reports in the field of analogue high-frequency electronics, one cannot leave it unnoticed that the performance of the industrial mainstream semiconductor fabrication technology-based devices, i.e., a CMOS and BiCMOS, now almost achieve the values of the benchmark-setting III/V devices. Although silicon-based devices are inherently slower, nevertheless, the cut-off frequencies f_T and the maximum oscillation frequencies f_{max} for modern FET and, in particular, silicon-germanium (SiGe) heterojunction bipolar transistors (HBTs) now are reported to exceed a 300 GHz barrier meaning that the devices can directly enter into the THz frequency range [14, 49]. A significant number of implementations rely on the efficient extraction of power generated at higher harmonics of a strong core

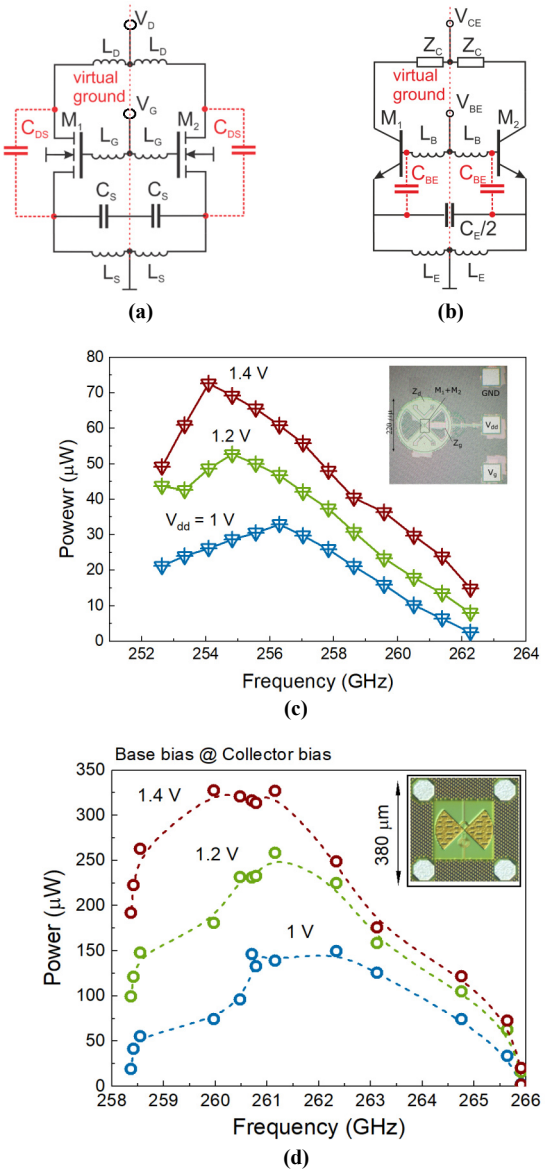

Fig. 5. Schematic representation of Colpitts oscillators: (a) for 65 nm CMOS technology and (b) for a 130 nm BiCMOS technology. Dependence of the radiated power on frequency which is controlled by gate (base) bias voltage when the drain-source (collector-emitter) bias voltage is set to 1 V (blue symbols), 1.2 V (green symbols) and 1.4 V (red symbols): (c) 65 nm CMOS VCO and (d) 130 nm BiCMOS technologies.

oscillator operating at frequencies that are typically optimized to be slightly below or close to the half of f_{max}, and the concomitant efficient extraction of radiation at one or a multitude of higher harmonics. Implementing a triple-push oscillator resulted in an on-wafer measured −7.9 dBm at 482 GHz frequency [50]. Owing to the high density of integration, a concept with coupled oscillators enabled the generation of −1.2 dBm at 290 GHz and −3.3 dBm at 320 GHz [51].

Even higher output powers are reported for implementations utilizing BiCMOS devices, resulting in 1 dBm from a single antenna at 245 GHz [52] or −6.3 dBm at 430 GHz [53]. In the same technology, the power combining technique for a 64-element array enabled the report of 9.2 dBm radiated power at 420 GHz [54]. A 1 Hz barrier was recently passed using an efficient power-combining approach with 42 oscillators, resulting in a total emitted power of −10.9 dBm at 1.01 THz [55].

For more information about the recent developments in the field of solid-state sources and detectors, it is advised to read a number of dedicated review articles like these which focus either on silicon technologies [56] or frequency multiplication with Schottky diodes [4], direct generation like with resonant-tunnelling diodes [18, 57] or present a broad-scale overview [58].

The following section of this article aims to demonstrate that the already achieved performance of silicon-based devices allows addressing most applications which have been used to prove the applicability of THz technologies fully with compact and cost-effective devices produced by the mainstream silicon fabrication technologies.

4. Source-detector systems

The availability of compact CMOS-based components [see Fig. 6(b)] enables the implementation of different experiments. Figure 7(a) shows the setup for a precise determination of the oscillator frequency by employing heterodyne mixing between the test source and the reference generator. The radiation from the emitter (either MOSFET or HBT-based) is overlapped using a beam-splitter with the tunable source based on the Schottky diode frequency multiplier chain (Virginia Diodes, Inc.). The spectra of the resulting mixing signal (left axis) are shown in Fig. 7(b). The left axis shows the dynamic range of the mixing signal, where the line appears when both frequencies are close to the same value. The linewidth of the signal is determined by the modulation bandwidth of the detector (currently limited by 4 MHz). The triangle symbols represent the measured frequency of oscillations as a function of base bias voltage (shown with the right axis).

The setup presented in Fig. 8(a) employs a compact electronic source (either MOSFET or HBT) and a broad-band spiral-antenna-coupled detector in a Michelson-type interferometer configuration. This approach allows to measure harmonics content of the emitted radiation. For the harmonic oscillator sources implemented in 65 nm CMOS [see the top panel of Fig. 4(c), one can clearly indicate the suppressed emission at the fundamental frequency of 88 GHz, the main radiation peak with the highest power at the third harmonic, i.e., 256 GHz, as well as emission at the second harmonic at 176 GHz (emission at this harmonic was expected to be suppressed due to circuit symmetry).

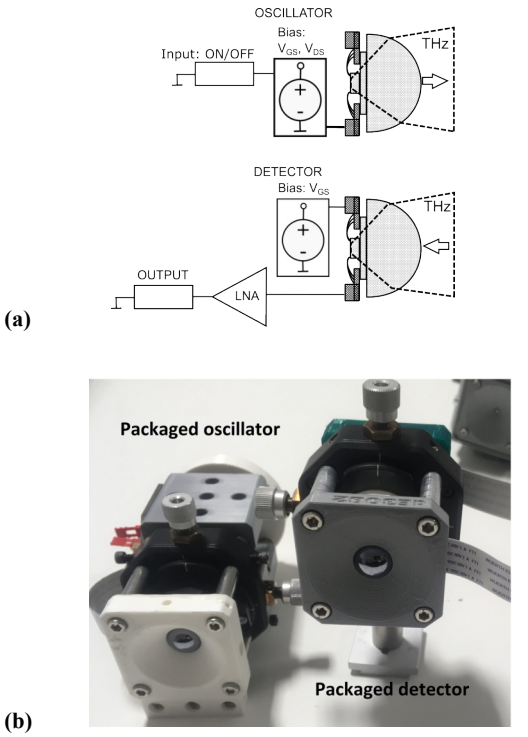

Fig. 6. (a) Schematic representation for the oscillator (top) and detector (bottom) assemblies. Both assemblies share a similar concept of construction: a hyper-hemispheric high resistivity silicon lens with a 12 mm diameter, a 500 µm thick undoped silicon substrate wafer which is glued to the printed circuit board with bonding pads and protection electronics [see also Fig. 1(d)]. (b) Photo of the packaged oscillator and detector modules.

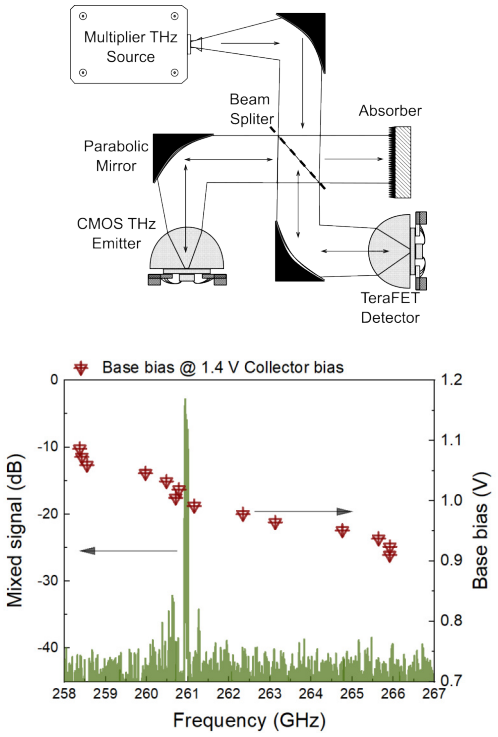

Fig. 7. (a) The setup for heterodyne mixing involves a VCO emitter (either an MOSFET or an HBT-based emitter), a tunable THz source based on a Schottky multiplier chain and beam splitter. (b) The dynamic range of mixing signal (left axis): the line appears when both frequencies are close in value. Frequency of oscillations (triangles) as a function of base bias voltage (for 130 nm BiCMOS VCO) is shown on the right axis.

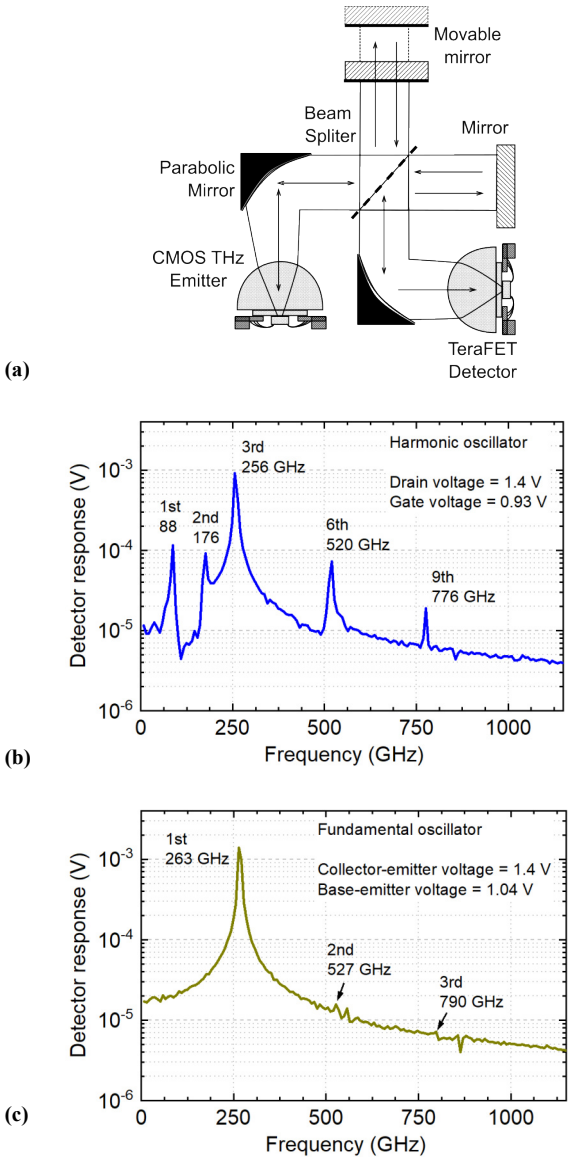

Fig. 8. (a) Schematic of the Fourier transform interferometer with a Si-based source-detector THz pair. The radiation spectra obtained using the interferometer for a 65 nm CMOS harmonic oscillator and a 130 nm SiGe HBT fundamental oscillator are shown in (b) and (c), respectively.

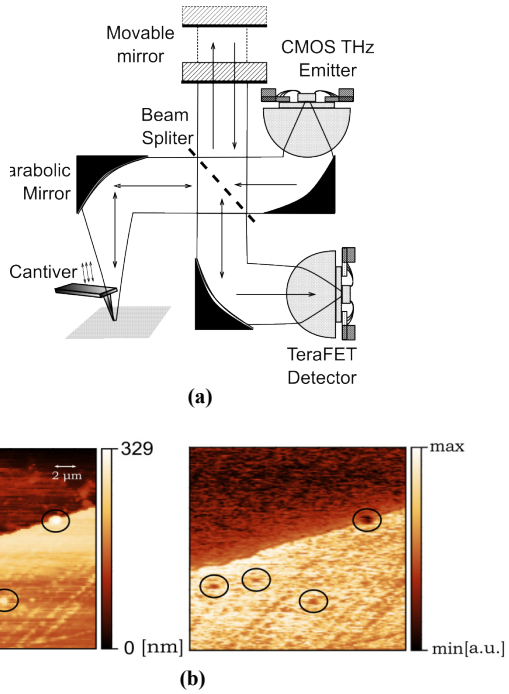

Fig.9. (a) Schematic of the setup used for near-field imaging; (b) left panel: 2-D topology of the gold-to-silicon interface measured by AFM; right panel: same area scanned using the 3rd harmonic of s-SNOM signal at the interface between gold (corresponding to max. values) and silicon (corresponding to low values). Marked are dust particles showing different contrast in AFM and s-SNOM modes.

There is a clear indication for the emission at the 6th harmonic at the frequency of 519 GHz with expected power levels of the order of a few μW. This spectral line can be utilized as well, provided that lower harmonics are effectively filtered. The cleanest emission spectrum can be obtained using an HBT-based fundamental oscillator, as presented in the lower panel of Fig. 8(b). Obtained spectrum has only the main radiation peak with higher harmonics being effectively suppressed by the device capacitance and antenna symmetry.

The CMOS-based emitter-detector pair was successfully utilized at the scattering-type scanning near-field optical microscopy (s-SNOM) setup [Fig. 9(a)]. The setup is built for homodyne measurements as in Ref. 59 but now it contains only compact THz-electronic devices. There are two beam paths in the interferometer: signal arm – THz radiation emitted by the source is collimated by a 4-inch parabolic mirror, 50% of radiation power passes through a beam-splitter and is focused by a 2-inch parabolic mirror onto an atomic force microscopy (AFM) tip, THz radiation scattered by the tip is collected by the same 2-inch mirror, reflected from the beam-splitter, it is then focused by a Teflon lens onto the THz detector; reference arm – THz radiation emitted by the source is collimated by a 4-inch parabolic mirror, 50% of radiation power is reflected by the beam-splitter and then reflected back from a flat mirror, the part of the radiation that passes through the beam-splitter is focused by a Teflon lens onto the THz detector and combined with the weak signal coming from the AFM tip (signal arm). In Fig. 9(b), both the AFM-measured topology and the s-SNOM image of the interface between gold and silicon can be seen. An area of 20×20 μm^2 with a total of $150 \times 150 = 22\,500$ pixels was scanned. Both images contain identical dust particles with a different contrast in AFM and s-SNOM modes.

The direct link between the emitter and detector (point-to-point connection, line-of-site, etc.) can be employed for imaging, as well as for wireless data transmission. We employ a simple on/off keying scheme in which the maximal rate of transmitted signals is mainly limited by the modulation bandwidth of the integrated low-noise amplifier at the detector side and the modulation speed or the divergence of radiation (so-called path loss) on the source side.

Our existing implementation of control electronics has a 100 MHz modulation rate. However, the limit of the systems modulation bandwidth is set by the input capacitance of amplifier of about 1 pF, which with the typical detector impedance of 4 kΩ results in $f_{3dB} \sim 40$ MHz.

The point-to-point configuration shown in Fig. 10(a) is a common schematic used for a THz transmission between an emitter and a detector. It is frequently utilized to achieve

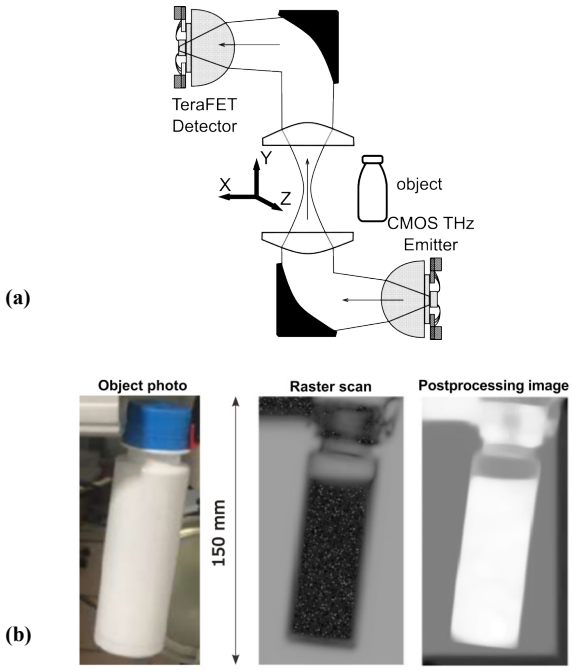

Fig. 10. (a) The point-to-point transmission system for raster-scan imaging at the position of intermediate focus. (b) Photo of optically opaque plastic bottle (left) with liquid inside. The central panel is a raster-scan THz image at 250 GHz. The right panel shows the result of numerical processing indicating the level of the liquid in the bottle.

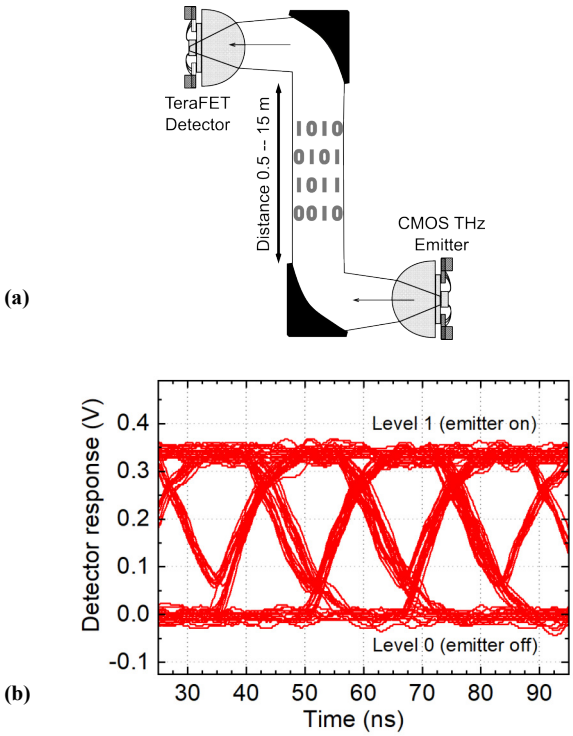

Fig. 11. (a) The point-to-point data transmission line. (b) The eye diagrams of the detector output signal at 3 MHz.

raster-scan images. As an example of such an application, the raster scan of an optically opaque plastic bottle was demonstrated. The left panel of Fig. 10(b) shows a photo of the object. The centre image is the intensity of the transmitted THz light in the raster scan. The raster scan in Fig. 10(b) has a resolution of 0.5 mm with a total of 140×260 pixels and a total scan time of approximately 18 minutes with a time constant of 10 ms. The scan time could be reduced by using a detector line or matrix. The right panel shows the result of numerical processing indicating the level of the liquid in the bottle.

The point-to-point configuration was also used as a free-space all-electronic THz communication system, as shown in Fig. 11(a). The system demonstrates an SNR ratio of 15.9 dB at a 32 MHz modulation frequency and the concomitant channel capacity of 266 MHz [see Fig. 11(b)]. The data transmission speed in the demonstration experiment is limited by the external electronic components used – the low-noise-amplifier and the modulator. However, according to the Shannon–Hartley theorem, the theoretical information capacity of the system without bandwidth limitation based on our core CMOS elements could be at least 100 Gbit/s per channel. Implementing state-of-the-art transmitter circuits should allow direct scaling of the throughput to 10 Gbit/s [60].

5. Conclusions

In summary, here the state-of-the-art of CMOS-based (MOSFET, as well as HBT) electronic sources and detectors developed for the THz frequency range was shortly presented. In particular, the antenna-coupled push-push type of oscillator that employs Colpitts configuration and emits up to 75 µW at 254 GHz (MOSFET-based harmonic oscillator) and 325 µW at 260 GHz (HBT-based fundamental oscillator) of power into the propagating beam was presented. The combination of this source and the substrate-lens coupled detectors allows implementing optical emitter-detector systems which exhibit input power-related signal-to-noise ratio above 70 dB in the direct detection regime for 1 Hz-equivalent noise bandwidth. The manuscript presents a variety of emitter–detector pairs that can be utilized in different experiments such as spectroscopy, data transmission, or near-field and raster-scan imaging.

Authors' statement

Research concept and design, D.B, K.I., C.K., and A.L.; collection data, A.C., A.K., K.I., and D.B.; data analysis and interpretation, D.B., K.I., and A.L.; writing the article, D.B., A.L., and K.I.; critical revision of the article, W.K. and H.R.; final approval of article, D.B. and A.L.

Acknowledgements

On the Polish side, the work was supported by the "International Research Agendas" program of the Foundation for Polish Science co-financed by the European Union under the European Regional Development Fund (No. MAB/2018/9) for CENTERA.

D. B. But acknowledges the funding from the European Union's Horizon 2020 research and innovation program under the grant agreement No. 857470.

The team from Germany acknowledges funding through the DFG-Fraunhofer-Cooperation program (project No. RO 770/43-1"TeraSpect").

The Lithuanian team acknowledges funding received from the Lithuanian Science Foundation (project No. S-MIP-22-83)

References

[1] Jepsen, P. U., Cooke, D. G. & Koch, M. Terahertz spectroscopy and imaging – Modern techniques and applications. *Laser Photon. Rev.* **5**, 124–166 (2011). https://doi.org/10.1002/LPOR.201000011

[2] Kürner, T., Mittleman, D. M. & Nagatsuma, T. Introduction to THz Communications. in *THz Communications* (eds. Kürner, T., Mittleman, D. M. & Nagatsuma, T.) 1–12 (Springer Science and Business Media Deutschland GmbH, 2022). https://doi.org/10.1007/978-3-030-73738-2_1

[3] Crowe, T. W., Porterfield, D. W. & Hesler, J. L. Multiplier-Based Sources of Terahertz Power. in *33rd International Conference on Infrared, Millimeter and Terahertz Waves, IRMMW-THz* 1 (IEEE, 2008). https://doi.org/10.1109/ICIMW.2008.4665442

[4] Siles, J. V., Cooper, K. B., Lee, C., Lin, R. H., Chattopadhyay, G. & Mehdi, I. A new generation of room-temperature frequency-multiplied sources with up to 10× higher output power in the 160-GHz-1.6-THz range. *IEEE Trans. Terahertz Sci. Technol.* **8**, 596–604 (2018). https://doi.org/10.1109/TTHZ.2018.2876620

[5] Pačebutas, V. *et al*. Terahertz time-domain-spectroscopy system based on femtosecond Yb:fiber laser and GaBiAs photoconducting components. *Appl. Phys. Lett.* **97**, 031111 (2010). https://doi.org/10.1063/1.3458826

[6] Deninger, A. J., Roggenbuck, A., Schindler, S. & Preu, S. 2.75 THz tuning with a triple-DFB laser system at 1550 nm and InGaAs photomixers. *J. Infrared Millim. Terahertz Waves* **36**, 269–277 (2015). https://doi.org/10.1007/s10762-014-0125-5

[7] Fernandes, L. O. T. *et al*. Photometry of THz Radiation Using Golay Cell Detector. in *2011 XXXth URSI General Assembly and Scientific Symposium* 1–4 (IEEE, 2011). https://doi.org/10.1109/URSIGASS.2011.6051287

[8] Absolute THz Power-Energy Meters. *TK Instruments Ltd*. (2018). http://www.terahertz.co.uk/tk-instruments/products/absolute-thz-power-energy-meters

[9] Judaschke, R. H., Kehrt, M., Kuhlmann, K. & Steiger, A. Linking the power scales of free-space and waveguide-based electromagnetic waves. *IEEE Trans. Instrum. Meas.* **69**, 9056–9061 (2020). https://doi.org/10.1109/TIM.2020.2998311

[10] Richards, P. L. Bolometers for infrared and millimeter waves, *J. Appl. Phys.* **76**, 1 (1994). https://doi.org/10.1063/1.357128

[11] Valušis, G., Lisauskas, A., Yuan, H., Knap, W. & Roskos, H. G. Roadmap of terahertz imaging 2021. *Sensors* **21**, 4092 (2021). https://doi.org/10.3390/s21124092

[12] Han, R. & Afshari, E. A CMOS high-power broadband 260-GHz radiator array for spectroscopy. *IEEE J. Solid-State Circuits* **48**, 3090–3104 (2013). https://doi.org/10.1109/JSSC.2013.2272864

[13] Javadi, E. *et al*. Sensitivity of field-effect transistor-based terahertz detectors. *Sensors* **21**, 2909 (2021). https://doi.org/10.3390/s21092909

[14] Hillger, P., Grzyb, J., Jain, R. & Pfeiffer, U. R. Terahertz Imaging and sensing applications with silicon-based technologies. *IEEE Trans. Terahertz Sci. Technol.* **9**, 1–19 (2019). https://doi.org/10.1109/TTHZ.2018.2884852

[15] Nellen, S. *et al*. Experimental comparison of UTC- and PIN-photodiodes for continuous-wave terahertz generation. *J. Infrared Millim. Terahertz Waves* **41**, 343–354 (2020). https://doi.org/10.1007/s10762-019-00638-5

[16] Sizov, F. Terahertz radiation detectors: the state-of-the-art *Semicond. Sci. Technol.* **33**, 123001 (2018). https://doi.org/10.1088/1361-6641/aae473

[17] Roser, H. P. *et al*. GaAs Schottky diodes for THz mixing applications. *Proc. IEEE*. **80**, 1827–1841 (1992). https://doi.org/10.1109/5.175258

[18] Feiginov, M. Frequency limitations of resonant-tunnelling diodes in Sub-THz and THz oscillators and detectors. *J. Infrared Millim. Terahertz Waves* **40**, 365–394 (2019). https://doi.org/10.1007/s10762-019-00573-5

[19] Boppel, S. *et al*. CMOS integrated antenna-coupled field-effect transistors for the detection of radiation from 0.2 to 4.3 THz. *IEEE Trans. Microw. Theory Tech.* **60**, 3834–3843 (2012). https://doi.org/10.1109/SiRF.2012.6160142

[20] Zak, A. *et al*. Antenna-integrated 0.6 THz FET direct detectors based on CVD graphene. *Nano Lett.* **14**, 5834–5838 (2014). https://doi.org/10.1021/nl5027309

[21] Viti, L. *et al*. Thermoelectric graphene photodetectors with sub-nanosecond response times at terahertz frequencies. *Nanophotonics* **10**, 89–98 (2020). https://doi.org/10.1515/nanoph-2020-0255

[22] Auton, G. *et al*. Terahertz detection and imaging using graphene ballistic rectifiers. *Nano Lett.* **17**, 7015–7020 (2017). https://doi.org/10.1021/acs.nanolett.7b03625

[23] Garg, S. *et al*. InGaAs self-switching diode-based THz bridge rectifier. *Semicond. Sci. Technol.* **36**, 075017 (2021). https://doi.org/10.1088/1361-6641/ABFFE0

[24] Qiu, Q. *et al*. High sensitivity of room-temperature terahertz photodetector based on silicon. *IScience* **25**, 105217 (2022). https://doi.org/10.1016/J.ISCI.2022.105217

[25] Gayduchenko, I. *et al*. Tunnel field-effect transistors for sensitive terahertz detection. *Nat. Commun.* **12**, 543 (2021). https://doi.org/10.1038/s41467-020-20721-z

[26] Dyakonov, M. I. Generation and detection of terahertz radiation by field effect transistors. *Comptes Rendus Phys.* **11**, 413–420 (2010). https://doi.org/10.1016/j.crhy.2010.05.003

[27] Knap, W. *et al*. Field effect transistors for terahertz detection: Physics and first imaging applications. *J. Infrared Millim. Terahertz Waves* **30**, 1319–1337 (2009). https://doi.org/10.1007/s10762-009-9564-9

[28] Lisauskas, A. *et al*. Rational design of high-responsivity detectors of terahertz radiation based on distributed self-mixing in silicon field-effect transistors. *J. Appl. Phys.* **105**, 114511 (2009). https://doi.org/10.1063/1.3140611

[29] Dyakonov, M. & Shur, M. Detection, mixing, and frequency multiplication of terahertz radiation by two-dimensional electronic fluid. *IEEE Trans. Electron Devices* **43**, 380–387 (1996). https://doi.org/10.1109/16.485650

[30] Ikamas, K. *et al*. Broadband terahertz power detectors based on 90-nm silicon CMOS transistors with flat responsivity up to 2.2 THz. *IEEE Electron Device Lett.* **39**, 1413–1416 (2018). https://doi.org/10.1109/LED.2018.2859300

[31] Bauer, M. *et al*. High-sensitivity AlGaN/GaN HEMT terahertz detector with integrated broadband bow-tie antenna. *IEEE Trans. Terahertz Sci. Technol.* **9**, 430–444 (2019). https://doi.org/10.1109/TTHZ.2019.2917782

[32] Zdanevicius, J. *et al*. Field-effect transistor based detectors for power monitoring of THz quantum cascade lasers. *IEEE Trans. Terahertz Sci. Technol.* **8**, 613–621 (2018). https://doi.org/10.1109/TTHZ.2018.2871360

[33] Knap, W. *et al*. Field effect transistors for terahertz imaging. *Phys. Status Solidi C* **6**, 2828–2833 (2009). https://doi.org/10.1002/PSSC.200982562

[34] Al Hadi, R. *et al*. A 1 k-pixel video camera for 0.7–1.1 terahertz imaging applications in 65-nm CMOS. *IEEE J. Solid-State Circuits* **47**, 2999–3012 (2012). https://doi.org/10.1109/jssc.2012.2217851

[35] Ikamas, K., But, D. B. & Lisauskas, A. Homodyne spectroscopy with broadband terahertz power detector based on 90-nm silicon CMOS transistor. *Appl. Sci.* **11**, 412 (2021). https://doi.org/10.3390/app11010412

[36] Ikamas, K. *et al*. Sub-picosecond pulsed THz FET detector characterization in plasmonic detection regime based on autocorrelation technique. *Semicond. Sci. Technol.* **33**, 124013 (2018). https://doi.org/10.1088/1361-6641/AAE905

[37] Zagrajek, P. *et al*. Time resolution and dynamic range of field-effect transistor-based Terahertz detectors. *J. Infrared Millim. Terahertz Waves* **40**, 703–719 (2019). https://doi.org/10.1007/s10762-019-00605-0

[38] But, D. B., Javadi, E., Knap, W., Ikamas, K. & Lisauskas, A. Silicon Based Resonant Power Detector for 620 GHz. in *2020 23rd International Microwave and Radar Conference (MIKON)* 305–308 (IEEE, 2020). https://doi.org/10.23919/MIKON48703.2020.9253787

[39] Fernandes, C. A., Lima, E. B. & Costa, J. R. Dielectric lens antennas. in *Handbook of Antenna Technologies* (eds. Chen, Z., Liu, D., Nakano, H., Qing, X. & Zwick, T.) 1001–1064 (Springer, 2016). https://doi.org/10.1007/978-981-4560-44-3_40

[40] Krysl, A. *et al*. Control and Optimization of Patch-Antenna-Coupled THz Detector Performance using Superstrate Dielectric and Silicon Lens. in *2022 47th International Conference on Infrared, Millimeter and Terahertz Waves (IRMMW-THz)* 1–2 (IEEE, 2022). https://doi.org/10.1109/IRMMW-THZ50927.2022.9896100

[41] Seok, E. *et al*. A 410GHz CMOS Push-Push Oscillator with an On-Chip Patch Antenna. in *2008 IEEE International Solid-State Circuits Conference – Digest of Technical Papers* 472–629 (IEEE, 2008). https://doi.org/10.1109/ISSCC.2008.4523262

[42] Seok, E. *et al*. Progress and challenges towards terahertz CMOS integrated circuits. *IEEE J. Solid-State Circuits* **45**, 1554–1564 (2010). https://doi.org/10.1109/JSSC.2010.2049793

[43] Huang, D. *et al*. Terahertz CMOS frequency generator using linear superposition technique. *IEEE J. Solid-State Circuits* **43**, 2730–2738 (2008). https://doi.org/10.1109/JSSC.2008.2004868

[44] Razavi, B. A 300-GHz fundamental oscillator in 65-nm CMOS technology. *IEEE J. Solid-State Circuits* **46**, 894–903 (2011). https://doi.org/10.1109/JSSC.2011.2108122

[45] Grzyb, J., Zhao, Y. & Pfeiffer, U. R. A 288-GHz lens-integrated balanced triple-push source in a 65-nm CMOS technology *IEEE J. Solid-State Circuits* **48**, 1751–1761 (2013). https://doi.org/10.1109/JSSC.2013.2253403

[46] But, D. B. *et al*. Silicon-based all-electronic quasi-optical pairs for THz frequency range. *Proc. SPIE* **12230**, 86–95 (2022). https://doi.org/10.1117/12.2633904

[47] Zhao, Y. *et al*. A 0.56 THz phase-locked frequency synthesizer in 65 nm CMOS technology. *IEEE J. Solid-State Circuits* **51**, 3005–3019 (2016). https://doi.org/10.1109/JSSC.2016.2601614

[48] Ikamas, K. *et al*. All-electronic emitter-detector pairs for 250 GHz in silicon. *Sensors* **21**, 5795 (2021). https://doi.org/10.3390/S21175795

[49] Schmid, R. L., Ulusoy, A. C., Zeinolabedinzadeh, S. & Cressler, J. D. A comparison of the degradation in RF performance due to device interconnects in advanced SiGe HBT and CMOS technologies. *IEEE Trans. Electron Devices* **62**, 1803–1810 (2015). https://doi.org/10.1109/TED.2015.2420597

[50] Momeni, O. & Afshari, E. High power terahertz and millimeter-wave oscillator design: A systematic approach. *IEEE J. Solid-State Circuits* **46**, 583–597 (2011). https://doi.org/10.1109/JSSC.2011.2104553

[51] Tousi, Y. M., Momeni, O. & Afshari, E. A novel CMOS high-power terahertz VCO based on coupled oscillators: Theory and implementation. *IEEE J. Solid-State Circuits* **47**, 3032–3042 (2012). https://doi.org/10.1109/JSSC.2012.2217853

[52] Schmalz, K., Wang, R., Borngräber, J., Debski, W., Winkler, W. & Meliani, C.245 GHz SiGe Transmitter With Integrated Antenna and External PLL. in *2013 IEEE MTT-S International Microwave Symposium Digest (MTT)* 1–3 (IEEE, 2013). https://doi.org/10.1109/MWSYM.2013.6697430

[53] Hillger, P., Grzyb, J., Malz, S., Heinemann, B. & Pfeiffer, U. A Lens-Integrated 430 GHz SiGe HBT Source With Up To −6.3 dBm Radiated Power. in *2017 IEEE Radio Frequency Integrated Circuits Symposium (RFIC)* 160–163 (2017). https://doi.org/10.1109/RFIC.2017.7969042

[54] Jain, R., Hillger, P., Ashna, E., Grzyb, J. & Pfeiffer, U. R. A 64-pixel 0.42-THz source soc with spatial modulation diversity for computational imaging. *IEEE J. Solid-State Circuits* **55**, 3281–3293 (2020). https://doi.org/10.1109/JSSC.2020.3018819

[55] Hu, Z., Kaynak, M. & Han, R. high-power radiation at 1 Thz in silicon: a fully scalable array using a multi-functional radiating mesh structure. *IEEE J. Solid-State Circuits* **53**, 1313–1327 (2018). https://doi.org/10.1109/JSSC.2017.2786682

[56] Hillger, P., Grzyb, J., Jain, R. & Pfeiffer, U. R. Terahertz imaging and sensing applications with silicon-based technologies. *IEEE Trans. Terahertz Sci. Technol.* **9**, 1–19 (2019). https://doi.org/10.1109/TTHZ.2018.2884852

[57] Asada, M. & Suzuki, S. Terahertz emitter using resonant-tunneling diode and applications. *Sensors* **21**, 1384 (2021). https://doi.org/10.3390/S21041384

[58] Aniel, F. *et al*. Terahertz Electronic Devices. in: *Springer Handbook of Semiconductor Devices*. (eds. Rudan, M., Brunetti, R. & Reggiani, S.) 807–849 (Springer, 2023). https://doi.org/10.1007/978-3-030-79827-7_22/COVER

[59] Wiecha, M. M. *et al*. Antenna-coupled field-effect transistors as detectors for terahertz near-field microscopy. *Nanoscale Adv.* **3**, 1717–1724 (2021). https://doi.org/10.1039/D0NA00928H

[60] Cesiul, A. *et al*. Towards wireless data transmission with compact all-electronic THz source and detector system. *Lith. J. Phys.* **62**, 127–137 (2022). https://doi.org/10.3952/PHYSICS.V62I3.4796